https://doi.org/10.1016/j.ijhydene.2019.11.221

Three-dimensional simulation of solid oxide fuel cell with metal foam as cathode flow distributor

Ruobing Zhan[a], Yang Wang[a], Meng Ni[b], Guobin Zhang[a], Qing Du[a,]*, Kui Jiao[a,]*

[a]State Key Laboratory of Engines, Tianjin University,

135 Yaguan Road, Tianjin, China, 300350

[b]Building Energy Research Group, Department of Building and Real Estate,

The Hong Kong Polytechnic University, Hung Hom, Kowloon, Hong Kong, China

*Corresponding author: kjiao@tju.edu.cn (K. Jiao); duqing@tju.edu.cn (Q. Du)

tel: +86-22-27404460; fax: +86-22-27383362

Abstract

In this study, the use of metal foam as a flow distributor at cathode is evaluated numerically by a comprehensive three-dimensional solid oxide fuel cell (SOFC) model. The results show that the adoption of metal foam improves the power density by 13.74% at current density of 5000 A m^{-2} in comparison with conventional straight channel design. It is found that electronic overpotential, oxygen concentration and reaction rates distribute more uniformly without the restriction of ribs. The effects of cathode thickness on the two different flow distributors are compared. Compared with conventional straight channel, the metal foam is found to be more suitable as a distributor for anode supported SOFC with thin cathode gas diffusion layer. Moreover, when metal foam is applied to the fuel cell with a larger reaction area, a more uniform velocity distribution and a lower temperature distribution can be achieved. It is also found that an appropriate permeability coefficient should offer a reasonable pressure drop, which is beneficial for the fuel cell system performance improvement.

Keywords: Solid oxide fuel cell; Metal foam; Three-dimensional model; Flow distributor.

Nomenclature

A	Area, m^2
A_v	Reactive surface area per unit volume, m^2 m^{-3}
c_p	Specific heat capacity, kJ kg^{-1} K^{-1}
D	Gas diffusivity, m^2 s^{-1}
E	Reversible voltage, V
F	Faraday's constant, C mol^{-1}
ΔG	Gibbs free energy change, J mol^{-1}
H	Heat of internal reforming reaction, J mol^{-1}
J	Current density, A m^{-2}
j	Exchange current density, A m^{-3}
K	Permeability, m^2
K_{pr}	MSR reaction equilibrium constant
K_{ps}	WGSR reaction equilibrium constant
k_{rf}	MSR forward reaction rate constant
k_{sf}	WGSR forward reaction rate constant
l	Thickness, μm
M	Molecular weight, kg mol^{-1}
MW	Average molar mass, kg mol^{-1}
N	Mole flow rate, mol s^{-1}
P	Pressure, Pa
P_{net}	Net power density, W
R	Universal gas constant, J mol^{-1} K^{-1}
S	Source term, kg m^{-3} s^{-1}, mol m^{-3} s^{-1} or W m^{-3}
T	Temperature, K
V	Special Fuller diffusion volume, cm^{-3} mol^{-1}
V_{out}	Output voltage, V
v	Velocity, m s^{-1}

x	Mole fraction
y	Mass fraction

Greek letters

α	Anode transfer coefficient
β	Cathode transfer coefficient
ε	Porosity
φ_{ele}	Electric potential, V
φ_{ion}	Ionic potential, V
η	Overpotential, V
γ	Adjustable parameter
ρ	Density, kg m^{-3}
κ	Thermal conductivity, W m^{-1} K^{-1}
σ	Conductivity, S m^{-1}
μ	Fluid viscosity, kg m^{-1} s^{-1}
ξ	Mechanical efficiency

Subscripts and superscripts

0	Standard state
a	Anode
act	Activation
ADL	Anode gas diffusion layer
c	Cathode
CDL	Cathode gas diffusion layer
eff	Effective
ele	Electron
i, j	Gas species
ion	Ion
I	Interface
k	Hydrogen oxygen reaction order
m	Oxygen reaction order

MSR	Methane steam reforming reaction
n	Carbon monoxide reaction order
ohm	Ohmic
ref	Reference state
WGSR	Water gas shift reaction

1. Introduction

Due to the high operating temperature (400-1000 °C), solid oxide fuel cell (SOFC) enables direct internal reforming of most hydrocarbon fuels in the anode thus is highly fuel flexible [1]. Thus, SOFC is regarded as a potential technology for future combined heat and power (CHP) cogeneration industry [2, 3]. Compared to tubular-type SOFC, planar-type designs have broader applications owing to the lower electrical resistance thus higher performance. And the compact structure makes it easier to be integrated into a stack. So far, the planar SOFCs can be divided into four types, including anode-supported, cathode-supported, electrolyte-supported and metal-supported SOFCs, among which the anode-supported SOFC is most widely applied in industry [4, 5].

An anode-supported SOFC contains five components: anode, cathode, electrolyte and two planar interconnects [6]. Since the interconnect is composed of flow channels and ribs, it plays important roles in both current collection and gas transfer, which tend to impact the cell performance through the ohmic polarization and concentration polarization [7]. Considering that the anode-supported SOFCs always adopt comparatively thin cathodes, it is usually more difficult for gas and electrons to distribute uniformly in the porous cathode. So the optimal design of interconnects is a significant field of SOFC research. Both the uniform gas distribution and current distribution should be taken into consideration to improve cell performance.

Some researchers focused on the transport characteristics of different flow field designs. Deepra et al. [8] found that serpentine flow field has higher fuel utilization and more uniform current distribution than parallel design. Saied et al. [9] compared several kinds of flow fields, including helical, parallel and multiple-entry serpentine flow fields, and the triple-entry serpentine design was found to achieve better cell performance and more uniform reactants distributions. Besides, many researchers proposed many optimized flow field designs [10-12] to get more uniform distributions of gas and current. Jakob et al. [10] attached a distributed channel on the gas inlet of the parallel flow field. Qu et al. [11] designed a corrugated bipolar plate with relatively wider air channels. And a new flow field design with a fan-shaped distribution of inlet channels was proposed by Danilov et al. [12]. These optimizations mentioned above improve the uniformity of gas and electrons in the cell, but the flow fields consist of rib and channel, which still have some restrictions on transports. Thus, other researchers focused on the optimization of interconnect geometry parameters. Lin et al.[13] illustrated the relation between the rib width and concentration polarization, and it is found that the best width of rib was estimated to be the 1/3 to 2/3 of the channel width. Julio et al [14] investigated the effects of the channel-electrode connect area on the cell output performance. The cell is found to achieve the best performance when the ratio of channel and electrode area was about 0.36. Liu et al. [15] established a numerical model considering the contact resistance of ribs. The results showed that the optimal rib width was linearly dependent with the pitch width. Another similar work was done by Li et al. [16] and similar conclusion was made. In the conventional flow filed designs, the phenomenon of low reactants concentration and low current density under rib can't be completely avoided, especially in thin cathode [17], which can significantly decrease the overall cell performance.

To overcome the restrictions of ribs and channel, the metal foam replaced flow distributors can be utilized in cell flow field. Adopting a porous flow distributor has a lot of advantages in terms of electrical conductivity and heat and mass transfer. In recent researches, as an emerging medium with high porosity, metal foam flow fields have been applied widely in proton exchange membrane fuel cells (PEMFCs). Great quantities of experiments [18, 19] and simulations [20-24] have verified the significant effects of metal foam distributor on reducing electrical resistance and enhancing gas transport, improving heat management and water removal. As for SOFCs, metal foam has been widely utilized as anode in the metal-supported structure [25]. Many metal porous materials [26, 27] have been developed to adapt to SOFC working condition. Unlike anode, the cathode of SOFC is in a strong oxidizing atmosphere. Zielke et al. [28] has experimentally investigated the cell performance degradation with Cu-Mn foam as cathode contact material. It was found that Cu-Mn foam can meet the requirements of long-term operation. This proved that Cu-Mn foam could be a suitable cathode distributor of SOFCs.

Meanwhile, there are very few numerical simulations focusing on SOFCs with the effect of porous material distributor. Iwai et al. [29] employed a porous material as a flow distributor to facilitate the flow distribution uniformity and current collection of SOFC. Wei et al. [30] used porous media current collector as cathode flow distributor to get uniform thermal-fluid-electrical properties, and the maximum power density and cell efficiency were remarkably increased. However, these pioneering studies lack detailed analysis of the mechanism of electrons transport, heat transfer and gas diffusion in the conventional flow and metal foam distributor. More importantly, the influence of property parameters of metal foam wasn’t taken into account.

To fill in the research gap, in this study, metal foam is applied to replace cathode flow channel. A comprehensive 3D computational fluid dynamics model of an anode-supported SOFC is developed to compare conventional straight channel and foam distributor. The improvements of metal foam on SOFC performance are analyzed in detail. The polarization curves and distributions of oxygen concentration, overpotential and electrochemical reaction rate are compared to evaluate the two different gas distributors. And the influences of cathode thickness, metal foam permeability and flow fields on the two different cases are investigated.

2. Numerical modeling

2.1 Model description and assumptions

Fig.1 shows the schematic of an anode-supported SOFC unit. Considering the symmetry structure, only half of a single channel is taken into account in the computation domain to improve the computation efficiency. As shown in Fig.1, two different cases are considered as follows:

Case A: A SOFC unit with two traditional straight channels on both anode and cathode is shown in Fig.1(a).

Case B: A SOFC unit with metal foam substituting for the channel and rib on cathode is shown in Fig.1(b).

These two cases are identical in geometry and compositions except the part of cathode gas distributor, which consist of anode and cathode interconnects, gas distributors (channel/metal foam), anode/cathode diffusion layers (ADL/CDL), anode/cathode catalyst layers (ACL/CCL) and electrolyte (ELE). The material is Ni/YSZ for ADL, Ni/ScSZ for ACL, dense ScSZ for electrolyte and LSM/ScSZ composite for cathode [31]. The geometry parameters are shown in Table 1. The cell parameters and physical properties are listed in Table 2 [32-39].

Besides, it is worth mentioning that the fuel supplied is a mixture of methane, carbon monoxide and steam, which will diffuse in the porous medium with methane steam reforming reaction (MSR) and water gas shift reaction (WGSR) happening [29] :

MSR:

$$\mathrm{CH_4 + H_2O \leftrightarrow CO + 3H_2} \tag{1}$$

WGSR:

$$\mathrm{CO}+\mathrm{H_2O}\leftrightarrow\mathrm{CO_2}+\mathrm{H_2} \tag{2}$$

This model follow these basic assumptions:

1. The SOFC is operated at steady state;
2. All the gas species are regarded as ideal gas;.
3. The gas fluid in channels is laminar;
4. The electronic and ionic conductors are assumed to be isotropic and homogeneous;
5. Gas leakage and radiation heat transfer are neglected.

2.2 Conservation equations

During the operation of SOFC, the electrochemical reactions take place with the transport of mass, heat, momentum and charge simultaneously. In order to obtain the distributions of various physical parameters in SOFC, several conservation equations are applied to describe the transport phenomena, which are summarized in Table 3 [34]. And the corresponding source terms are listed in Table 4.

Due to the multi-component characteristic of SOFC, the Dusty Gas model is adopted to describe the three transfer mechanisms of molecular diffusion, Knudsen diffusion and convection. The Knudsen diffusion coefficient ($D_{\mathrm{k,ij}}$) [30] and the binary diffusion coefficient (D_{ij}) [34] can be expressed as below:

$$D_{\mathrm{k,i}}=\frac{4}{3}r\sqrt{\frac{8RT}{\pi M_{\mathrm{i}}}} \tag{3}$$

$$D_{\mathrm{ij}}=\frac{0.0101T^{1.75}}{p(\frac{2M_{\mathrm{i}}M_{\mathrm{j}}}{M_{\mathrm{i}}+M_{\mathrm{j}}})^{1/2}\left[V_{\mathrm{i}}^{1/3}+V_{\mathrm{j}}^{1/3}\right]^2} \tag{4}$$

where r denotes the average pore radius (μm), V is the diffusion volume (cm^{-3} mol^{-1}), M is the molecular weight (kg mol^{-1}).

The effective diffusion coefficient $D_{\mathrm{eff,ij}}$ is calculated as [34]:

$$D_{\mathrm{eff,ij}} = \begin{cases} \dfrac{1-x_{\mathrm{i}}}{\sum_{\mathrm{j}\neq\mathrm{i}} \dfrac{x_{\mathrm{j}}}{D_{\mathrm{ij}}}} & \text{In channels} \\ \dfrac{\varepsilon}{\tau}\left(\dfrac{1}{\dfrac{\sum_{\mathrm{j}\neq\mathrm{i}} \dfrac{x_{\mathrm{j}}}{D_{\mathrm{ij}}}}{1-x_{\mathrm{i}}} + \dfrac{1}{D_{\mathrm{k,i}}}}\right) & \text{In electrodes} \end{cases} \tag{5}$$

where x is the mole fraction, ε is the porosity, τ is the tortuosity.

2.3 Electrochemical model

When hydrogen or carbon monoxide is supplied as fuel, the open circuit potential are shown in the Eqn. (9) and Eqn. (10), which contain the concentration overpotential implicitly [41]:

$$E_{\mathrm{OCV,H_2}} = E^0_{\mathrm{H_2}} + \frac{RT}{2F}\ln\left[\frac{P^{\mathrm{I}}_{\mathrm{H_2}}\left(P^{\mathrm{I}}_{\mathrm{O_2}}\right)^{0.5}}{P^{\mathrm{I}}_{\mathrm{H_2O}}}\right] \tag{9}$$

$$E_{\mathrm{OCV,CO}} = E^0_{\mathrm{CO}} + \frac{RT}{2F}\ln\left[\frac{P^{\mathrm{I}}_{\mathrm{CO}}\left(P^{\mathrm{I}}_{\mathrm{O_2}}\right)^{0.5}}{P^{\mathrm{I}}_{\mathrm{CO_2}}}\right] \tag{10}$$

where E^0 is the open circuit voltage under the standard condition, which can be calculated according to Gibbs free energy (J mol^{-1}); F is the Faraday's constant; P is the partial pressure of each reactant at TPB (atm); and T is the temperature (K). R is the universal gas constant. Moreover, when a mixture of various gases is adopted as fuel, the open circuit voltage should be averaged to combine the impact from different fuels.

According to the Butler-Volmer equation, the electrochemical reaction rates can be formulated as follow:

$$J_{\mathrm{a}} = j_{\mathrm{0,a}}A_{\mathrm{v}}\left(\exp\left(\alpha\frac{2F\eta_{\mathrm{act,a}}}{RT}\right) - \exp\left(-(1-\alpha)\frac{2F\eta_{\mathrm{act,a}}}{RT}\right)\right) \tag{11}$$

$$J_c = j_{0,c} A_V \left(\exp\left(\beta \frac{4F\eta_{\mathrm{act,c}}}{RT} \right) - \exp\left(-(1-\beta) \frac{4F\eta_{\mathrm{act,c}}}{RT} \right) \right) \tag{12}$$

where η_{act} is the activation overpotential (V), j_0 is the exchange current density (A m^{-2}), which can be calculated as below:

$$j_{0,a}^{H_2} = \gamma_{a,H_2} \left(\frac{P_{H_2}}{P_{\mathrm{ref}}} \right)^{m} \exp\left(-\frac{E_{\mathrm{act,a}}}{RT} \right) \tag{13}$$

$$j_{0,a}^{CO} = \gamma_{a,CO} \left(\frac{P_{CO}}{P_{\mathrm{ref}}} \right)^{n} \exp\left(-\frac{E_{\mathrm{act,a}}}{RT} \right) \tag{14}$$

$$j_{0,c}^{O_2} = \gamma_{c,O_2} \left(\frac{P_{O_2}}{P_{\mathrm{ref}}} \right)^{k} \exp\left(-\frac{E_{\mathrm{act,c}}}{RT} \right) \tag{15}$$

where m, n, k are reaction orders, both m and n are set as 0.5, k is set as 0.25; γ is the adjustable parameter, according to the different reaction rates of hydrogen and carbon monoxide [41], the value of γ_{a,H_2} is set to be about 2.2 times the value of $\gamma_{a,co}$.

2.4 Chemical model

At the high operating temperature, the MSR and WGSR will catalyzed by the nickel (Ni) in the porous anode. Thus, the reactions are considered to principally occur in the porous anode. The reaction rates of MSR [43] and WGSR [44] can be calculated respectively as:

$$R_{\mathrm{MSR}} = k_{\mathrm{rf}} \left(p_{CH_4} p_{H_2O} - \frac{p_{CO} \left(p_{H_2} \right)^3}{K_{\mathrm{pr}}} \right) \tag{16}$$

$$R_{\mathrm{WGSR}} = k_{\mathrm{sf}} \left(p_{H_2O} p_{CO} - \frac{p_{H_2} p_{CO_2}}{K_{\mathrm{ps}}} \right) \tag{17}$$

where k_{rf} and k_{sf} are rate constants; K_{pr} and K_{ps} are equilibrium constants, both of which are temperature dependent and should be determined from experimental data.

The heat generation by two chemical reaction can be expressed as below [45]:

$$H_{\mathrm{MSR}} = -\left(206205.5 + 19.5175T \right) \tag{18}$$

$$H_{\mathrm{WGSR}} = 45063 - 10.28T \tag{19}$$

2.5 Boundary conditions

In this study, the SOFC is supposed to operate in galvanostatic mode. The overpotential on the terminal of cathode interconnect is set to zero, while the operating current density is specified at the anode terminal surface, so the output voltage can be obtained at the specified current.

The inlets are set to mass-flow inlet, the flow rates can be calculated as below [34]:

Anode: $$m_{\mathrm{a}} = N_{\mathrm{fuel}}^{0} MW_{\mathrm{fuel}} \tag{20}$$

Cathode: $$m_{\mathrm{c}} = N_{\mathrm{air}}^{0} MW_{\mathrm{air}} \tag{21}$$

where MW is the average molar mass (kg mol^{-1}).

The outlets are adopted as pressure outlet under the constant pressure of 1 atm. The thermal boundary condition of the surrounding walls is assumed to be adiabatic boundary with zero heat flux. And the temperature of inlet gas is the same as the operating temperature. Since the half of a cell is employed as computational domain, the symmetrical boundary condition is imposed.

2.6 Numerical procedures

As mentioned above, the comprehensive three-dimensional SOFC model contains seven governing equations for mass, energy, momentum, electron, ion and species transfer, and the conservation equations are solved by commercial CFD software Fluent. The user defined functions (UDF) are employed to solve the electronic and ionic transfer and species transport (we consider both diffusion and convection). To guarantee the consistency of_grid quality, both case A and case B shown in the Fig.1 have the same grid quantity of 10000, each layer of fuel cell unit is divided into 10 sections along the X directions, 10 sections along Y directions, 100 sections along Z directions. The grid independence check is carried out by changing the number of grid cells from 10 to 15 along both X and Y directions, and 100 to 150 along the Z directions, the difference of main simulation results (oxygen concentration, average current density, temperature) under different grids numbers is within 1%, which is negligible.

3.Results and discussion

3.1 Experimental comparison

The comparison between experiment data in [31] and simulation results is shown in Fig.2. The geometry structures and electrode materials are consistent with those in the experiment. The flow rates of fuel and oxygen are both 300 mL min^{-1} according to the experimental condition. Hydrogen and syngas (58.2%H_2, 3.07%H_2O, 19.4%CO, 19.4%CO_2) are respectively adopted as fuel in Fig2.(a) and Fig2.(b), and the two comparisons both proceed at three different temperatures (1023K, 1073K, 1123K).

The simulated polarization curves are found to reasonably agree with the experiment data, validating the comprehensive 3D model in the present study.

3.2 Comparison between case A and case B

3.2.1 Cell performance

The net power densities and polarization curves of the two cases are shown in the Fig.3. In order to evaluate the system performances of the two structures, the pumping power caused by pressure drop should be taken into account. The net power density can be formulated as below [45]:

$$P_{\mathrm{net}} = V_{\mathrm{out}} J - \Delta P v_{\mathrm{in}} A_{\mathrm{in}} / A_{\mathrm{act}} / \xi \tag{22}$$

where, V_{out} is the output voltage (V), J is the current density (A m^{-2}), ΔP is the pressure drop (Pa), v_{in} is the average inlet velocity (m s^{-1}), A_{in} is the inlet area (m^2), A_{act} is the active area (m^2), ξ is the mechanical efficiency, which is set as 70%.

As can been seen from Fig.3, there is a significant improvement by applying metal foam as a flow distributor. Owing to the higher pumping loss, the net power densities for case B are almost the same as case A at low current density. However, the power density for case B is significantly higher than that for case A at high current density, indicating improved reactant gas transfer to porous electrodes by the use of metal foam. The net power densities are improved by 11%~20% at high current density (more than 4000 A m^{-2}). At the current density of 5000 A m^{-2}, the output voltage of case B is 0.581 V, with a 13.74% enhancement of net power density compared to case A.

Fig.4 shows the distribution of electrical overpotential at 5000 A m^{-2}. The electric overpotential of case A varies from 0.3611V to 0.3657V at anode and 0.0052V to 0.0859V at cathode. While the electric overpotential of case B varies from 0.3186V to 0.3226V at anode and 0.00177V to 0.0194V at cathode. It can be observed that electric overpotential of case B is evidently more uniform and lower. The variations and distribution rules are similar at the anode of both two cases, but it shows remarkable distinction at cathode due to the different transport paths of electrons.

Since the electrons can only transport through the rib in conventional design, most electrons are forced to move horizontally in the cathode porous layer. The electrons need to travel a longer path from the rib to reach the porous cathode under the channel This causes higher ohmic loss for case A and thus higher electric overpotential under the cathode channel. The anode distribution of electric overpotential can be explained in a similar way. And the smaller variation of anode electric overpotential indicates that the loss can be reduced by thickening cathode, which is studied in the next section. However, when metal foam is applied as a gas distributor, the increase of electroconductive area enables the electrons to transport uniformly through the shortest path, and the high electrical conductivity further reduces the ohmic loss, which in turn leads to the better cell performance of case B in Fig.3.

3.2.2 Effect of cathode GDL thickness

In this section, cathode gas diffusion layer (CDL) with different thicknesses is applied in both cases. The effect of CDL thickness on the cell performance in the two models is suggested in Fig.5

In Fig.5, the output voltage of two models is plotted as a function of the CDL thickness under four current densities (2000, 4000, 6000, 8000 A m^{-2}). Compared to case B, it can be found that the CDL thickness plays a more important role in case A on the cell performance, especially at high current density. It is evident to observe that two cases perform differently with the change of CDL thickness. Optimal GDL thicknesses are observed for case A, as the SOFC voltage increases significantly with increasing GDL thickness and then decreases after reaching peak values. In contrast, the output voltages of case B under different current densities all decrease continuously with increasing CDL thickness. Under various current densities and various GDL thicknesses, the performance of SOFC using metal foam is always higher than that of conventional SOFC. For conventional anode supported SOFC with straight channels, thin cathode (0~50μm) is commonly adopted. However, the present simulation results suggest that the optimal GDL thickness to achieve maximum voltage is between 200µm to 300µm. But for SOFC with metal foam as gas distributor, the thinner CDL offers better cell performance, demonstrating that metal foam has the same functions with gas diffusion layers for the gas and electron transfer.

The distributions of oxygen concentration, activation overpotential and reaction rate with six different CDL thicknesses at middle cross section are discussed in Fig.6,7,8, respectively, where (a) represents for case A, (b) represents for case B.

In Fig.6 the horizontal width of fuel cell is applied as abscissa. The change trends of oxygen concentration distribution at different CDL thicknesses are compared. As Fig.6(a) shows, the oxygen concentration is relatively high and almost uniform under the channel, however, it starts to decline near the rib, and further decreases under the rib, especially for thin cathode. The very large difference in oxygen concentration under the channel and under the rib clearly demonstrates the importance of rib design. It is also clear that this oxygen concentration difference decreases significantly with increasing CDL thickness. In other words, the oxygen distribution uniformity is improved by increasing the CDL thickness, although the concentration loss is still significant. For comparison, the oxygen distribution is highly uniform in the cathode of SOFC with metal foam distributor, as shown in Fig.6(b). However, the diffusion resistance grows with the increase of CDL thickness, resulting in the slight reduction of oxygen concentration in Fig.6(b), which has similar change rule with the oxygen concentration under rib in Fig.6(a).

In the same way, the activation overpotential under different CDL thicknesses are suggested in Fig.7. The activation overpotential under rib is higher than under channel in Fig.7(a). And thicker CDL offers more uniform overpotential distribution. In Fig.7(b), the activation overpotential change slightly along the cell width but thicker CDL offers bigger activation overpotential. It’s noticeable that the activation overpotential shown in Fig.7(b) is lower than that in Fig.7(a) at each thickness of CDL.

Fig.8 shows the comparison of electrochemical reaction rates on the ELE/CCL interface. According to B-V equation, the reaction rate is influenced by both oxygen concentration and activation overpotential. Thus, all maximal rates at different CDL thicknesses all occur near the border of rib and channel in Fig.8(a), and then six curves fall down under rib, some fall to zero when oxygen runs out. Combining Fig.6(a) and Fig.7(a), a correlative relationship can be found. The oxygen concentration under rib is relatively lower due to the existence of rib inhibits oxygen transport, but the high overpotential facilitates the increase of reaction rate near the rib, which aggravates the depletion of oxygen under rib. This relationship is like a vicious circle, which makes oxygen depletion more severe at high current density and the outlet area. This situation can be alleviated by increasing CDL thickness to enhance the mass and electron transfer under rib. However, it should be emphasized that the thicker CDL is not always better. When the GDL thickness is more than 300μm, it brings more losses than benefits. The electrochemical reaction rates in Fig.8(b) change in small range along the cell width owing to the uniform distributions of both oxygen and overpotential. Similarly, the thinner CDL offers higher reaction rates. Because of the excellent mass and electron transfer capability of metal foam, the case B with metal foam as flow distributor has no specific requirement for CDL thickness. But the thickening of CDL slightly increases the ohmic and concentration loss, indicating that metal foam is more suitable to be a flow distributor for anode-supported SOFC with thin CDL. It should be mentioned that activation overpotential in Fig.7(b) and reaction rate in Fig.8(b) are slightly higher in the left side because the straight channel is still applied in the anode and the effect of rib cannot be completely eliminated.

3.3 Effect of permeability

As metal foam is adopted as gas distributor, the fuel cell performance will be influenced by the parameters of porous medium, such as the permeability coefficient, which determines the gas diffusion and pressure drop inside SOFC. The permeability of metal foam is mainly concentrated in the range of $1e^{-7}$ m^2 to $1e^{-10}$ m^2 [46]. In this section, the permeability coefficient is assigned as $1e^{-7}$, $1e^{-8}$, $1e^{-9}$ and $1e^{-10}$ m^2. The polarization curves at different permeability are shown in Fig.9(a). And the pressure drop along the flow direction are shown in Fig.9(b). It can be found that better performance is always accompanied with larger pressure drop. When permeability is reduced from $1e^{-7}$ m^2 to $1e^{-10}$ m^2 , the output voltage rises from 0.5796 V to 0.5958 V at 5000 A m^{-2}, but the pressure drop rises significantly from 206.7 Pa to 65500.4 Pa. The decrease of the permeability coefficient increases the flow resistance, giving rise to larger pressure drop losses which is far greater than the slight improvement of cell performance. Therefore, the permeability coefficient of porous material is beneficial to the improvement of cell performance.

3.4 Effects of flow field

The comparison of single channel has been discussed above, and the effects of flow field with larger reaction area are studied as well. A conventional parallel flow field and a metal foam flow field are applied at cathode of SOFCs with the same active area of 20mm×100mm, in which gas enter from a main inlet. Other detail geometry parameters and operating condition stay same with that in Table 1. The two flow fields are compared at the same current density of 5000 A m^{-2}.

The comparison of velocity distributions is shown in Fig.10(a). Both maximum velocities occur in the inlet area. It is evident that the metal foam flow field offers a more uniform velocity distribution without the constraint of ribs. In parallel flow field, the channels near the inlet have a greater velocity, illustrating the velocity distribution is largely depended on the size and position of inlet. But the flow field applying metal foam can mitigate the impact of that. Fig.10(b) shows the pressure distribution of two flow fields. The pressure of the channels close to inlet is higher than that of other channels. Due to the porous structures, it can be found that pressure drop will increase when metal foam is applied as distributor. The oxygen concentration distribution in the ELE/CCL interface of two different flow fields is shown in the Fig.11. The adoption of metal foam evidently improves the uniformity of oxygen distribution, which is similar to the conclusion in Fig.7 but more remarkable in large activation area. In addition, Fig.12 suggests the temperature distributions of SOFC with two different flow field. Both the operating temperature is set as 1073.15 K. The maximum temperatures are 1209.47 K and 1178.04 K in the SOFCs with parallel and metal foam flow field, respectively. Combined with the results of Fig.9, the high reaction rate around the rib leads to high current density, which is a significant heat generating raising temperature of SOFC with parallel flow field. On the other hand, since heat is transferred mainly through the interconnect at cathode [47] in the parallel flow field, the excellent heat conduction and larger heat transfer area of metal foam widen the temperature difference between the two flow fields. It is noticeable that higher temperature should have led to better performance, but SOFC with metal foam flow field retain higher output power at lower temperature.

4.Conclusion

In this study, metal foam is proposed to replace the conventional straight channel at cathode. A comprehensive 3D numerical model of an anode-supported SOFC is conducted to compare conventional straight channel and foam distributor. Compared with conventional channel design, the adoption of metal foam achieves better cell performance. The improvement of output voltage at base case can reach at 13.74%. The capability of mass transfer and electrical conductivity are enhanced when metal foam is applied, more uniform distributions of oxygen concentration, overpotential and reaction rates are offered, which reduce both concentration loss and ohmic loss. Moreover, the performance of anode-supported SOFC is found to be greatly affected by cathode thickness. For conventional channel design, the increase of CDL thickness improves the cell performance at first, then decrease slowly. Contrary to the common adoption of thin CDL (0~50 μm), the CDL thickness for maximum power density is around 300 μm at the specific case. However, the thickening of CDL degrades performance when using metal foam. A thinner GDL or being without GDL can reduce concentration loss instead, which demonstrates that metal foam has the same functions with gas diffusion layers on the gas and electron transfer. Therefore, metal foam is suitable to be used as a distributor for anode-supported SOFC adopting thin cathode gas diffusion layer. In addition, when metal foam applies to the fuel cell with larger reaction area, the larger mass transfer area can weaken the effect of the inlet design on flow field distribution. Due to the excellent heat conduction and uniform electrons transport, a lower and more uniform temperature distribution can be offered as well. Besides, the effect of permeability was investigated, the result shows that the metal foam with high permeability leads to better performance but accompanied with larger pressure drop, indicating that it is critical to select appropriate porous parameters to balance the improvement and loss.

Acknowledgements

This work is supported by the National Key Research and Development Program of China (2017YFB0601904). M. Ni thanks the funding support (Project Number: PolyU 152214/17E) from Research Grant Council, University Grants Committee, Hong Kong SAR.

Reference

[1] Ni M, Zhao TS. Solid Oxide Fuel Cells: From Materials to System Modeling. Royal Society of Chemistry, Print ISBN: 978-1-84973-654-1; PDF eISBN: 978-1-84973-777-7.

[2] Damo U M, Ferrari M L, Turan A, Solid oxide fuel cell hybrid system: A detailed review of an environmentally clean and efficient source of energy[J]. Energy, 2019, 168:235-246

[3] Cottrell CA, Grasman SE, Thomas M, Martin KB, Sheffield JW. Strategies for stationary and portable fuel cell markets. International Journal of Hydrogen Energy, 2011;36(13):7969e75.

[4] Suwanwarangkul R, Croiset E, Fowler M W, et al. Performance Comparison of Fick's, Dusty-Gas and Stefan-Maxwell Models to Predict the Concentration Overpotential of a SOFC Anode[J]. Journal of Power Sources, 2003, 122(1):9-18.

[5] Lin B, Shi Y, Cai N. Numerical simulation of cell-to-cell performance variation within a syngas-fuelled planar solid oxide fuel cell stack[J]. Applied Thermal Engineering, 2017, 114:653-662.

[6] Ramadhani F, Hussain M A, Mokhlis H, et al. Optimization strategies for Solid Oxide Fuel Cell (SOFC) application: A literature survey[J]. Renewable & Sustainable Energy Reviews, 2017, 76:460-484.

[7] Huang C M, Shy S S, Lee C H. On flow uniformity in various interconnects and its influence to cell performance of planar SOFC[J]. Journal of Power Sources, 2008, 183(1):205-213.

[8] Bhattacharya D, Mukhopadhyay J, Biswas N, et al. Performance evaluation of different bipolar plate designs of 3D planar anode-supported SOFCs[J]. International Journal of Heat and Mass Transfer, 2018, 123:382-396.

[9] M. Saied, K. Ahmed, M. Nemat-Alla, M. Ahmed, M. El-Sebaie. Performance study of solid oxide fuel cell with various flow field designs: numerical study[J]. International Journal of Hydrogen Energy, 2018, 43(46):20931-20946.

[10] Duhn J D, Jensen A D, Wedel S, et al. Optimization of a new flow design for solid oxide cells using computational fluid dynamics modelling[J]. Journal of Power Sources, 2016, 336:261-271.

[11] Qu Z, Aravind P V, Boksteen S Z, et al. Three-dimensional computational fluid dynamics modeling of anode-supported planar SOFC[J]. International Journal of Hydrogen Energy, 2011, 36(16):10209-10220.

[12] Danilov V A, Tade M O. A CFD-based model of a planar SOFC for anode flow field design[J]. International Journal of Hydrogen Energy, 2009, 34(21):8998-9006.

[13] Lin Z, Stevenson J W, Khaleel M A. The effect of interconnect rib size on the fuel cell concentration polarization in planar SOFCs[J]. Journal of Power Sources, 2003, 117(1):92-97.

[14] Moreno-Blanco J, Elizalde-Blancas F, Riesco-Avila J M, et al. On the effect of gas channels-electrode interface area on SOFCs performance[J]. International Journal of Hydrogen Energy, 2018.

[15] Liu S, Song C, Lin Z. The effects of the interconnect rib contact resistance on the performance of planar solid oxide fuel cell stack and the rib design

optimization[J]. Journal of Power Sources, 2008, 183(1):214-225.

[16] Li X, Shi Y, et al. Optimization of interconnect flow channels width in a planar solid oxide fuel cell[J]. International Journal of Hydrogen Energy, 2018, 43(46):13738-13750.

[17] Zhang G, Jiao K. Multi-phase models for water and thermal management of proton exchange membrane fuel cell: A review[J]. Journal of Power Sources, 2018, 391:120-133.

[18] Tseng C J, Heush Y J, Chiang C J, et al. Application of metal foams to high temperature PEM fuel cells[J]. International Journal of Hydrogen Energy, 2016, 41(36):16196-16204.

[19] Dong K S, Jin H Y, Dong G K, et al. Effect of Cell Size in Metal Foam Inserted to the Air Channel of Polymer Electrolyte Membrane Fuel Cell for High Performance[J]. Renewable Energy, 2017, 115.

[20] Jo A, Ju H. Numerical study on applicability of metal foam as flow distributor in polymer electrolyte fuel cells (PEFCs)[J]. International Journal of Hydrogen Energy, 2018, 43(30): 14012-14026.

[21] Toghyani S, Afshari E, Baniasadi E. Metal foams as flow distributors in comparison with serpentine and parallel flow fields in proton exchange membrane electrolyzer cells[J]. Electrochimica Acta, 2018, 290:506-519

[22] Afshari E, Mosharaf-Dehkordi M, Rajabian H. An investigation of the PEM fuel cells performance with partially restricted cathode flow channels and metal foam as a flow distributor[J]. Energy, 2017, 118:705-715.

[23] Li S, Sunden B. Three-dimensional modeling and investigation of high temperature proton exchange membrane fuel cells with metal foams as flow distributor[J]. International Journal of Hydrogen Energy, 2017, 42(44): 27323-27333.

[24] Jo A, Ahn S, Oh K, et al. Effects of metal foam properties on flow and water distribution in polymer electrolyte fuel cells (PEFCs)[J]. International Journal of Hydrogen Energy, 2018.

[25] Tan WC, Saw LH, Thiam HS, et al. Overview of porous media/metal foam application in fuel cells and solar power systems[J]. Renewable and Sustainable Energy Reviews. 2018, 96:181-197

[26] Gondolini A, Mercadelli E, Sangiorgi A, et al. Integration of Ni-GDC layer on a NiCrAl metal foam for SOFC application[J]. Journal of the European Ceramic Society, 2017, 37(3):1023-1030.

[27] Pang Q, Gaohui W U, Sun D, et al. Compressive property and energy absorption characteristic of 3D open-cell Ni–Cr–Fe alloy foams under quasi-static conditions[J]. Transactions of Nonferrous Metals Society of China, 2012, 22(Suppl 2):s566-s572.

[28] Zielke P, Wulff A C, Sun X, et al. Investigation of a Spinel-forming Cu-Mn Foam as an Oxygen Electrode Contact Material in a Solid Oxide Cell Single Repeating Unit[J]. Fuel Cells, 2017, 17(5).

[29] Iwai H, Yamamoto Y, Saito M, et al. Numerical simulation of intermediate-temperature direct-internal-reforming planar solid oxide fuel cell[J]. Energy, 2011, 36(4):2225-2234.

[30] Wei S S, Wang T H, Wu J S. Numerical modeling of interconnect flow channel design and thermal stress analysis of a planar anode-supported solid oxide fuel cell stack[J]. Energy, 2014, 69:553-561.

[31] Li W, Shi Y, Luo Y, et al. Elementary reaction modeling of solid oxide electrolysis cells: Main zones for heterogeneous chemical/electrochemical reactions[J]. Journal of Power Sources, 2015, 273:1-13.

[32] Shi Y , Cai N , Li C , et al. Modeling of an anode-supported Ni-YSZ vertical bar Ni-ScSZ vertical bar ScSZ vertical bar LSM-ScSZ multiple layers SOFC cell - Part I. Experiments, model development and validation[J]. Journal of Power Sources, 2007, 172(1):235-245.

[33] Shi Y, Wang H, Cai N. Direct two-dimensional electrochemical impedance spectra simulation for solid oxide fuel cell. Journal of Power Sources, 2012, 208: 24-34.

[34] Wang Y, Zhan R, et al.Three-dimensional modeling of pressure effect on operating characteristics and performance of solid oxide fuel cell. International Journal of Hydrogen Energy, 2018, 43(43): 20059-20076.

[35] Park J, Kim Y M, Bae J. Electrochemical simulation using material properties of a ceramic electrode and electrolyte. Current Applied Physics, 2011, 11(1): S219-S222.

[36] Fourie J G, Plessis J P D. Pressure drop modelling in cellular metallic foams[J]. Chemical Engineering Science, 2002, 57(14):2781-2789.

[37] Ni M. The effect of electrolyte type on performance of solid oxide fuel cells running on hydrocarbon fuels. International Journal of Hydrogen Energy, 2013, 38(6): 2846-2858.

[38] Choudhary T. Computational analysis of IR-SOFC: Transient, thermal stress, carbon deposition and flow dependency. International Journal of Hydrogen Energy, 2016, 41(24): 10212-10227.

[39] Ni M. Modeling of SOFC running on partially pre-reformed gas mixture. International Journal of Hydrogen Energy, 2012, 37(2): 1731-1745.

[40] Fuller E N, Schettler P D, Giddings J C. New method for prediction of binary gas-phase diffusion coefficients. Industrial & Engineering Chemistry, 1966, 58(5): 18-27.

[41] Ni M. Electrolytic effect in solid oxide fuel cells running on steam/methane mixture. Journal of Power Sources, 2011, 196(4): 2027-2036.

[42] Recknagle K P, Ryan E M, Koeppel B J, et al. Modeling of electrochemistry and steam–methane reforming performance for simulating pressurized solid oxide fuel cell stacks. Journal of Power Sources, 2010, 195(19): 6637-6644.

[43] Haberman B A, Young J B. Three-dimensional simulation of chemically reacting gas flows in the porous support structure of an integrated-planar solid oxide fuel cell. International Journal of Heat and Mass Transfer, 2004, 47(17-18): 3617-3629.

[44] Gholaminezhad I, Paydar M H, Jafarpur K, et al. Multi-scale mathematical

modeling of methane-fueled SOFCs: Predicting limiting current density using a modified Fick's model. Energy Conversion and Management, 2017, 148: 222-237.

[45] Ni M. 2D thermal modeling of a solid oxide electrolyzer cell (SOEC) for syngas production by H2O/CO2 co-electrolysis. International Journal of Hydrogen Energy, 2012, 37(8): 6389-6399.

[46] Carton J. Representative model and flow characteristics of open pore cellular foam and potential use in proton exchange membrane fuel cells[J]. International Journal of Hydrogen Energy, 2015, 40(16):5726-5738.

[47] Lee S, Park M, Kim H, et al. Thermal conditions and heat transfer characteristics of high-temperature solid oxide fuel cells investigated by three-dimensional numerical simulations[J]. Energy, 2017, 120:293-305.

Figure and table captions

Figure 1. Schematic diagram of SOFC with two different flow distributors.

Figure 2. Comparison between the simulation results and the experiment data [31]. (a) H_2 as fuel; (b) Syngas as fuel.

Figure 3. Polarization curves and power densities of two cases.

Figure 4. Electric overpotential distribution of two different cases (a) case A; (b) case B.

Figure 5. Effect of CDL thickness on cell performance of two cases.

Figure 6. Oxygen concentration distributions on the middle of ELE/CCL interface at different CDL thicknesses. (a) case A; (b) case B.

Figure 7. Activation overpotential distributions on the middle of ELE/CCL interface at different CDL thicknesses. (a) case A; (b) case B.

Figure 8. Reaction rate distributions on the middle of ELE/CCL interface at different CDL thicknesses. (a) case A; (b) case B.

Figure 9. Effect of foam permeability at current density of 5000 A m^{-2}. (a) on the cell performance; (b) on the pressure drop.

Figure 10. Velocity and pressure distributions of two different cathode flow fields. (a) velocity distribution. (b) pressure distribution.

Figure 11. Oxygen concentration distributions on the ELE/CCL interface of two different flow fields.

Figure 12. Temperature distributions of SOFC with two different flow fields.

Table 1. Cell geometry.

Table 2. Operating conditions and physical properties.

Table 3. Conservation equations.

Table 4. Source terms.

Table 1 Cell geometry.

Parameters	Value
Channel length (mm)	100
Channel height (mm)	1
Channel width (mm)	1.25
Metal foam length (mm)	100
Metal foam height (mm)	1
Metal foam width (mm)	2
Rib width (mm)	0.75
Interconnect thickness (mm)	1
Anode diffusion layer thickness (μm)	500
Cathode diffusion layer thickness (μm)	40
Anode catalyst layer thickness (μm)	10
Cathode catalyst layer thickness (μm)	10
Electrolyte thickness (μm)	10

Table 2 Operating conditions and physical properties.

Parameters	Value
Anode transfer coefficient [32]	0.33
Cathode transfer coefficient [32]	0.33
Anode activation energy (kJ mol^{-1}) [33]	110
Cathode activation energy (kJ mol^{-1}) [33]	130
Porosity of anode, cathode, foam [34, 36]	0.3, 0.3, 0.9
Tortuosity of anode, cathode, foam [35, 36]	6.0, 6.0, 2.3
Permeability of anode, cathode, foam [34, 36]	1.76e^{-11}, 1.76e^{-11}, 1e^{-8}
Thermal conductivity of anode, cathode, electrolyte, foam, interconnect (W m^{-1} K^{-1}) [35, 38]	11, 6.0, 2.7 ,90, 20
Electronic conductivity of anode (S m^{-1})[36]	$\frac{9.5\times10^{7}}{T}\exp\left(\frac{-1150}{T}\right)$
Electronic conductivity of cathode (S m^{-1}) [36]	$\frac{4.2\times10^{7}}{T}\exp\left(\frac{-1200}{T}\right)$
Ionic conductivity of electrolyte(S m^{-1}) [33]	$6.92\times10^{4}\exp\left(\frac{-9681}{T}\right)$
Operating pressure (atm)	1.0
Operating temperature (K)	1073
Inlet temperature of gas (K)	1073
operation current density (A m^{-2})	5000
Flow arrangement	Co-flow
Fuel utilization	0.7
Air ratio [38]	9.0
Fuel composition [39]	26.3% H_2, 49.3% H_2O, 17.1% CH_4, 2.94% CO, 4.36% CO_2
Air composition	21% O_2, 79% N_2

Table.3. Conservation equations.

Description	Governing Equation	Computational domain
Mass	$\nabla\cdot\left(\varepsilon\rho v\right)=S_{\mathrm{m}}$	Anode/Cathode Channel, Anode/Cathode GDL, Anode/Cathode CL
Species	$\nabla\cdot\left(-\rho y_{\mathrm{i}}\sum_{\mathrm{j}\neq\mathrm{i}}^{\mathrm{n}}D_{\mathrm{eff,ij}}\nabla x_{\mathrm{j}}+\rho v y_{\mathrm{i}}\right)=S_{\mathrm{i}}$	Anode/Cathode Channel, Anode/Cathode GDL, Anode/Cathode CL
Momentum	$\nabla\cdot\left(\varepsilon\rho v v\right)=-\varepsilon\nabla p+\nabla\cdot\left[\varepsilon\mu\left(\nabla v+\left(\nabla v\right)^{\mathrm{T}}\right)\right]+S_{\mathrm{u}}$	Anode/Cathode Channel, Anode/Cathode GDL, Anode/Cathode CL
Energy	$\nabla\cdot(\varepsilon\rho c_{\mathrm{p}}vT)=\nabla\cdot\left(\kappa_{\mathrm{eff}}\nabla T\right)+S_{\mathrm{T}}$	All domains
Electronic charge	$0=\nabla\cdot\left(\sigma_{\mathrm{ele}}^{\mathrm{eff}}\nabla\varphi_{\mathrm{ele}}\right)+S_{\mathrm{ele}}$	Anode/Cathode Interconnect, Anode/Cathode GDL, Anode/Cathode CL
Ionic charge	$0=\nabla\cdot\left(\sigma_{\mathrm{ion}}^{\mathrm{eff}}\nabla\varphi_{\mathrm{ion}}\right)+S_{\mathrm{ion}}$	Anode/Cathode CL, electrolyte

Table 4 Source terms.

Source terms	Unit
$S_{\mathrm{m}}=\begin{cases}0 & \text{Channels}\\ S_{\mathrm{CH_4}}+S_{\mathrm{H_2}}+S_{\mathrm{CO}}+S_{\mathrm{H_2O}}+S_{\mathrm{CO_2}} & \text{ADL/ACL}\\ S_{\mathrm{O_2}} & \text{CCL}\end{cases}$	$\mathrm{kg\ m^{-3}\ s^{-1}}$
$S_{\mathrm{CH_4}}=-R_{\mathrm{MSR}}M_{\mathrm{CH_4}}\qquad \text{ADL/ACL}$	$\mathrm{kg\ m^{-3}\ s^{-1}}$
$S_{\mathrm{H_2}}=\begin{cases}(3R_{\mathrm{MSR}}+R_{\mathrm{WGSR}})M_{\mathrm{H_2}} & \text{ADL}\\ (3R_{\mathrm{MSR}}+R_{\mathrm{WGSR}})M_{\mathrm{H_2}}-\dfrac{J_{\mathrm{H_2}}}{2F}M_{\mathrm{H_2}} & \text{ACL}\end{cases}$	$\mathrm{kg\ m^{-3}\ s^{-1}}$
$S_{\mathrm{CO}}=\begin{cases}(R_{\mathrm{MSR}}-R_{\mathrm{WGSR}})M_{\mathrm{CO}} & \text{ADL}\\ (R_{\mathrm{MSR}}-R_{\mathrm{WGSR}})M_{\mathrm{CO}}-\dfrac{J_{\mathrm{CO}}}{2F}M_{\mathrm{CO}} & \text{ACL}\end{cases}$	$\mathrm{kg\ m^{-3}\ s^{-1}}$
$S_{\mathrm{H_2O}}=\begin{cases}(-R_{\mathrm{MSR}}-R_{\mathrm{WGSR}})M_{\mathrm{H_2O}} & \text{ADL}\\ (-R_{\mathrm{MSR}}-R_{\mathrm{WGSR}})M_{\mathrm{H_2O}}+\dfrac{J_{\mathrm{H_2O}}}{2F}M_{\mathrm{H_2O}} & \text{ACL}\end{cases}$	$\mathrm{kg\ m^{-3}\ s^{-1}}$
$S_{\mathrm{CO_2}}=\begin{cases}R_{\mathrm{WGSR}}M_{\mathrm{CO_2}} & \text{ADL}\\ R_{\mathrm{WGSR}}M_{\mathrm{CO_2}}+\dfrac{J_{\mathrm{CO_2}}}{2F}M_{\mathrm{CO_2}} & \text{ACL}\end{cases}$	$\mathrm{kg\ m^{-3}\ s^{-1}}$
$S_{\mathrm{O_2}}=-\dfrac{J_{\mathrm{O_2}}M_{\mathrm{O_2}}}{2F}\qquad \text{CCL}$	$\mathrm{kg\ m^{-3}\ s^{-1}}$
$S_{\mathrm{u}}=\begin{cases}0 & \text{Channels}\\ -\dfrac{\mu}{K}\varepsilon^2 v & \text{ADL,ACL,CCL,CDL}\end{cases}$	$\mathrm{kg\ m^{-2}\ s^{-2}}$
$S_{\mathrm{T}}=\begin{cases}\lVert\nabla\varphi_{\mathrm{ele}}\rVert\kappa_{\mathrm{ele}}^{\mathrm{eff}} & \text{Interconnects, CDL}\\ \lVert\nabla\varphi_{\mathrm{ion}}\rVert\kappa_{\mathrm{ion}}^{\mathrm{eff}} & \text{ELE}\\ 0 & \text{Channels}\\ \lVert\nabla\varphi_{\mathrm{ele}}\rVert\kappa_{\mathrm{ele}}^{\mathrm{eff}}+R_{\mathrm{MSR}}H_{\mathrm{MSR}}+R_{\mathrm{WGSR}}H_{\mathrm{WGSR}} & \text{ADL}\\ \lVert\nabla\varphi_{\mathrm{ele}}\rVert\kappa_{\mathrm{ele}}^{\mathrm{eff}}+\lVert\nabla\varphi_{\mathrm{ion}}\rVert\kappa_{\mathrm{ion}}^{\mathrm{eff}}+J_{\mathrm{a}}\lvert\eta_{\mathrm{act}}^{\mathrm{a}}\rvert+J_{\mathrm{a}}\dfrac{\Delta S_{\mathrm{a}}T}{2F} & \\ +R_{\mathrm{MSR}}H_{\mathrm{MSR}}+R_{\mathrm{WGSR}}H_{\mathrm{WGSR}} & \text{ACL}\\ \lVert\nabla\varphi_{\mathrm{ele}}\rVert\kappa_{\mathrm{ele}}^{\mathrm{eff}}+\lVert\nabla\varphi_{\mathrm{ion}}\rVert\kappa_{\mathrm{ion}}^{\mathrm{eff}}+J_{\mathrm{c}}\lvert\eta_{\mathrm{act}}^{\mathrm{c}}\rvert+J_{\mathrm{c}}\dfrac{\Delta S_{\mathrm{c}}T}{4F} & \text{CCL}\end{cases}$	$\mathrm{W\ m^{-3}}$

$S_{\mathrm{ele}} = \begin{cases} -J_{\mathrm{a}} \\ J_{\mathrm{c}} \end{cases}$	ACL CCL	A m^{-3}
$S_{ion} = \begin{cases} J_{\mathrm{a}} \\ -J_{\mathrm{c}} \end{cases}$	ACL CCL	A m^{-3}

Figure

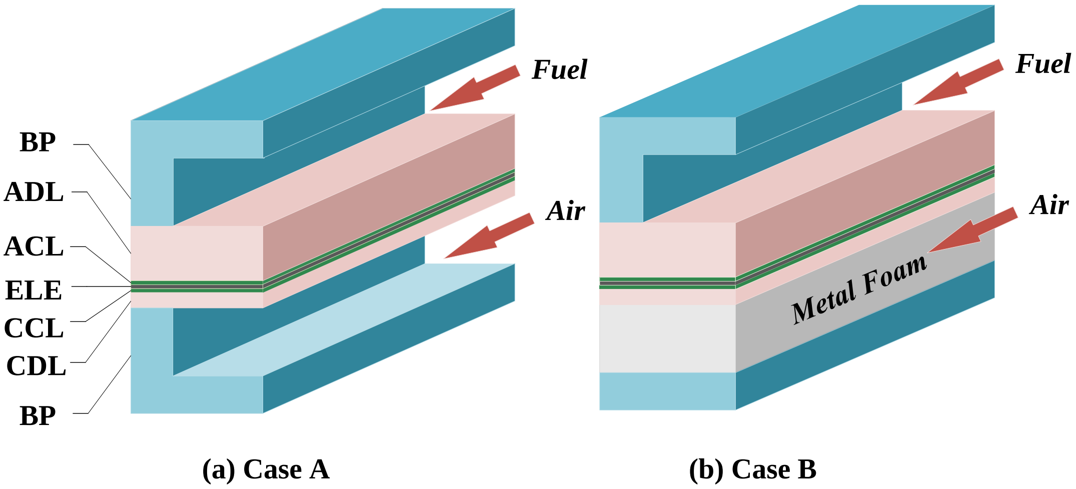

(a) Case A

(b) Case B

Fig. 1 Schematic diagram of SOFC with two different flow distributors.

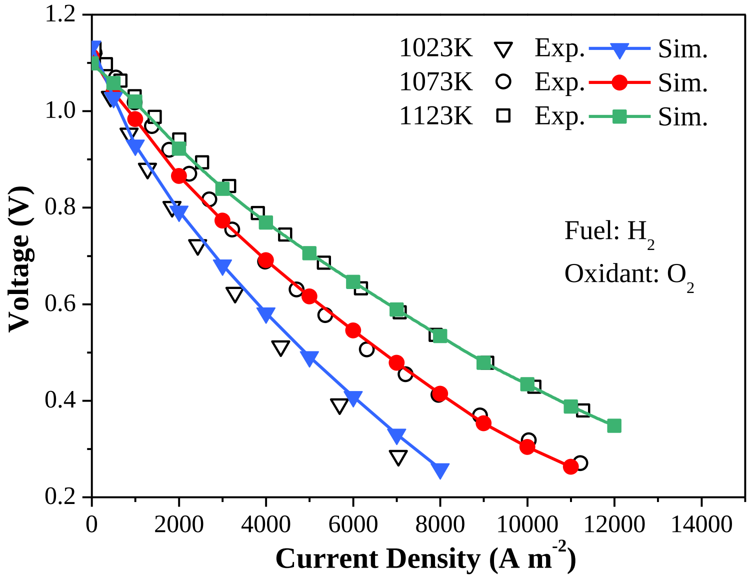

(a)

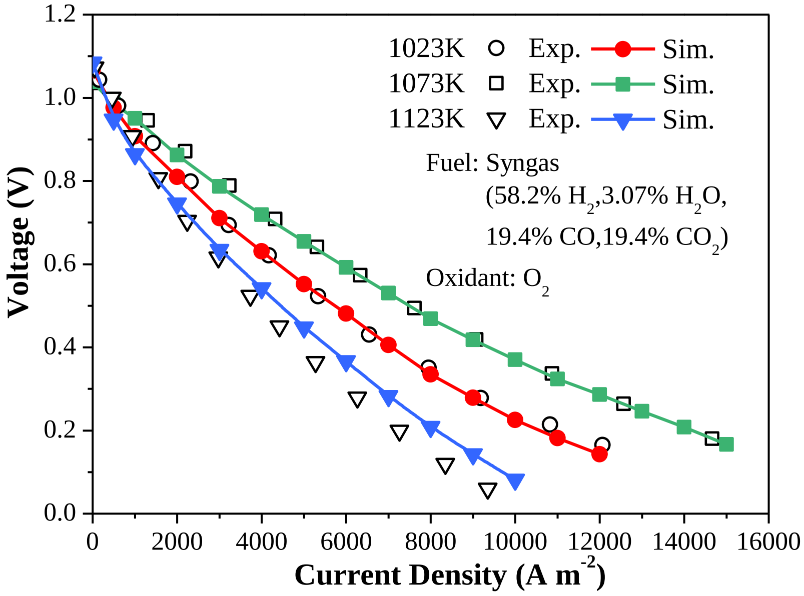

(b)

Fig.2 Comparison between the simulation results and the experiment data [31].
(a) H_2 as fuel; (b) syngas as fuel.

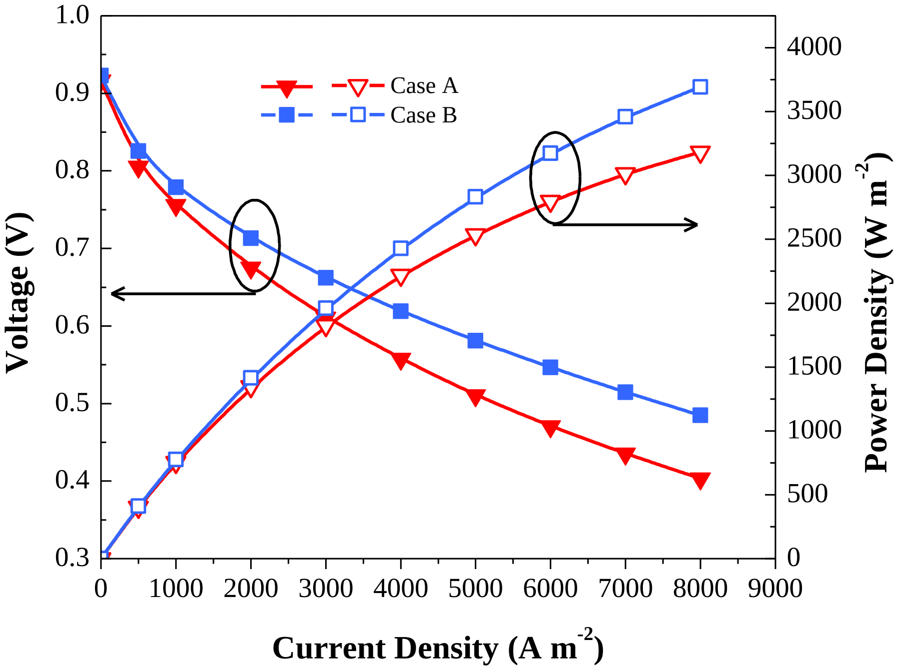

Fig.3 Polarization curves and power densities of two cases.

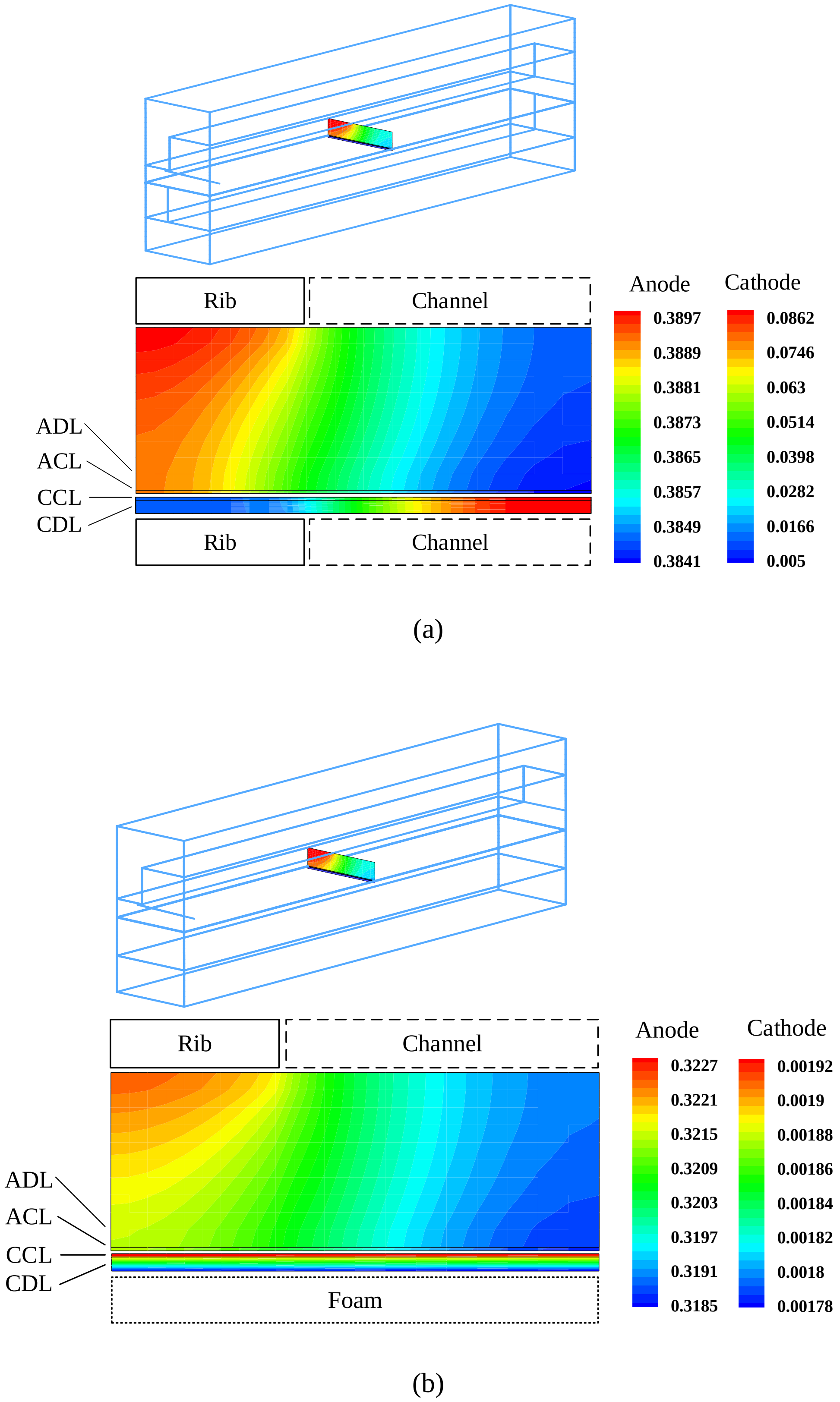

Fig.4 Electric overpotential distribution of two different cases
(a) case A (b) case B

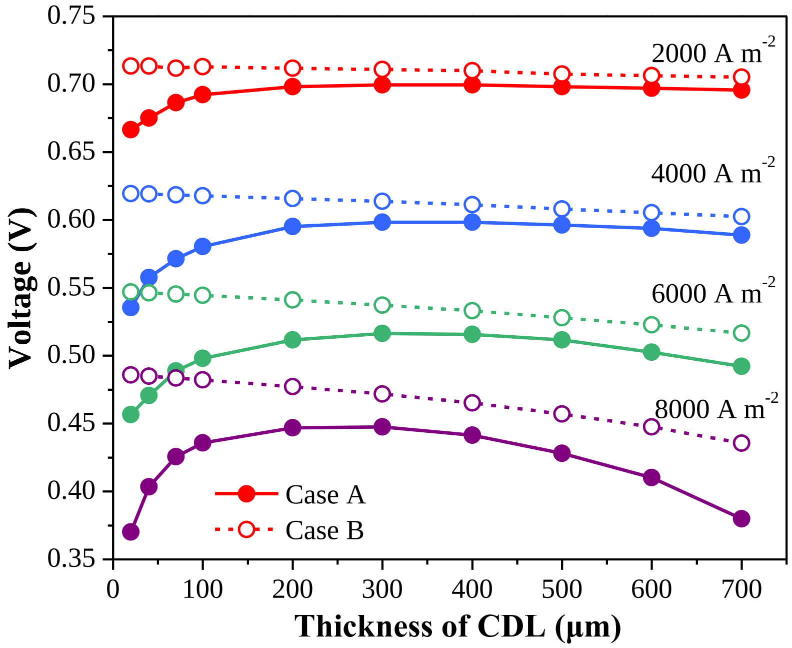

Fig.5 Effect of CDL thickness on cell performance of two cases.

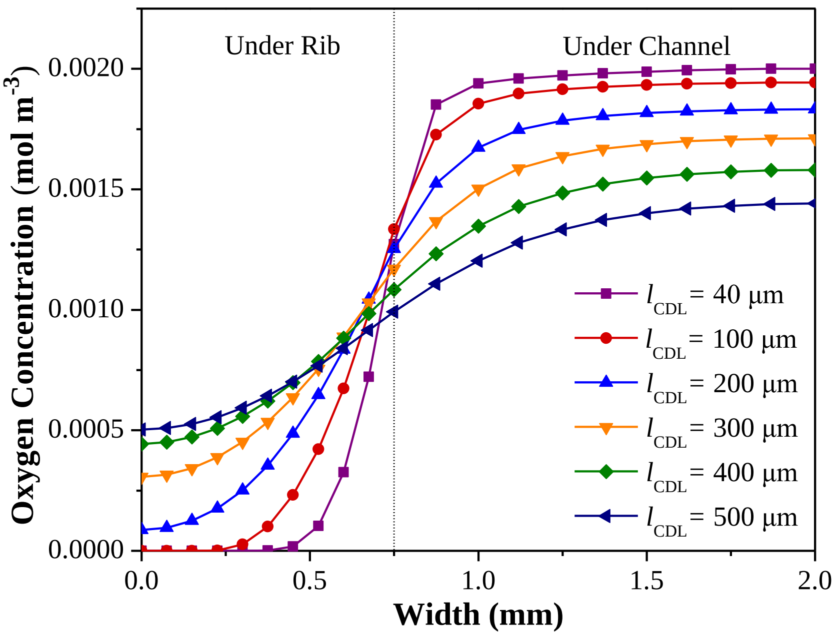

(a)

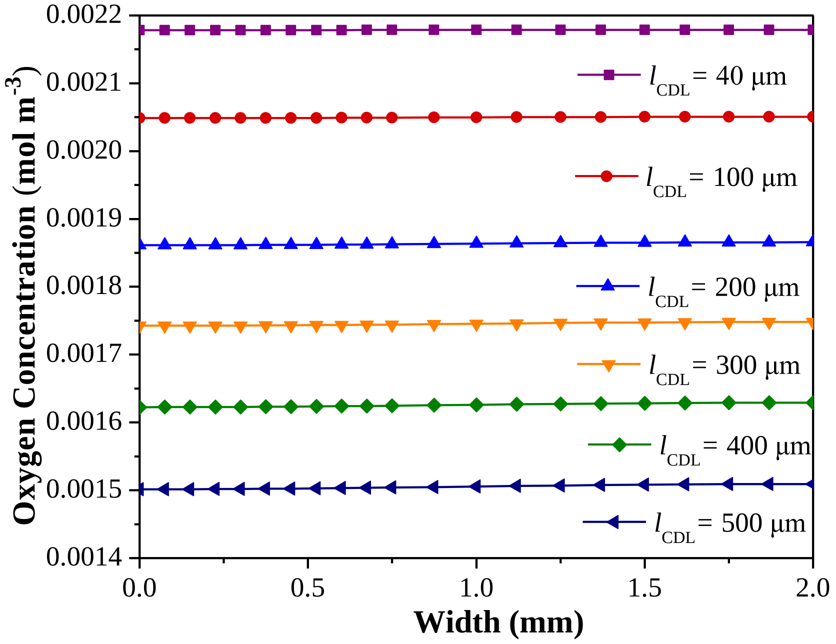

(b)

Fig.6 Oxygen concentration distribution on the middle of ELE/CCL interface at different CDL thickness.

(a) case A (b) case B

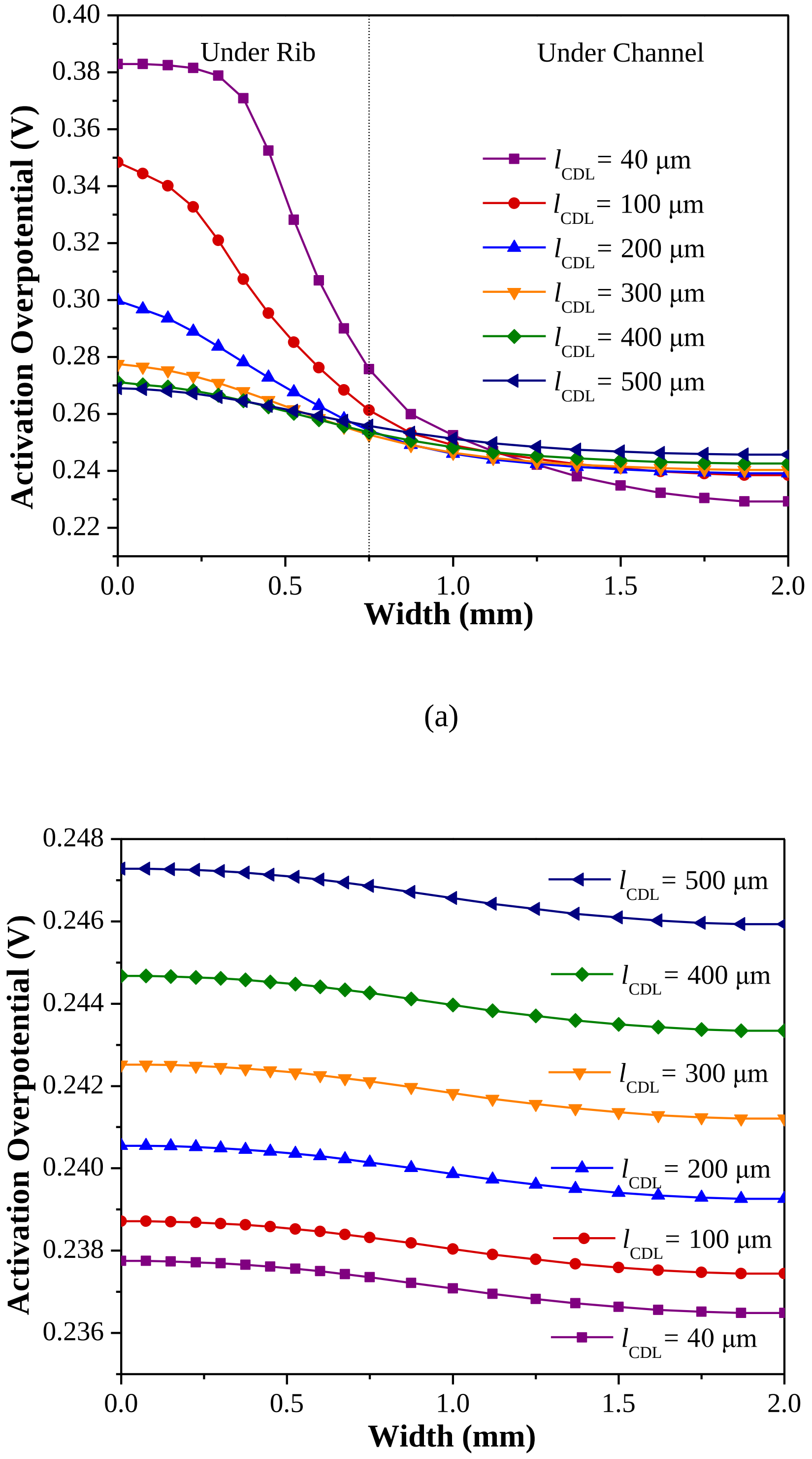

(a)

(b)

Fig.7 Activation overpotential distribution on the middle of ELE/CCL interface at different CDL thickness.

(a) case A (b) case B

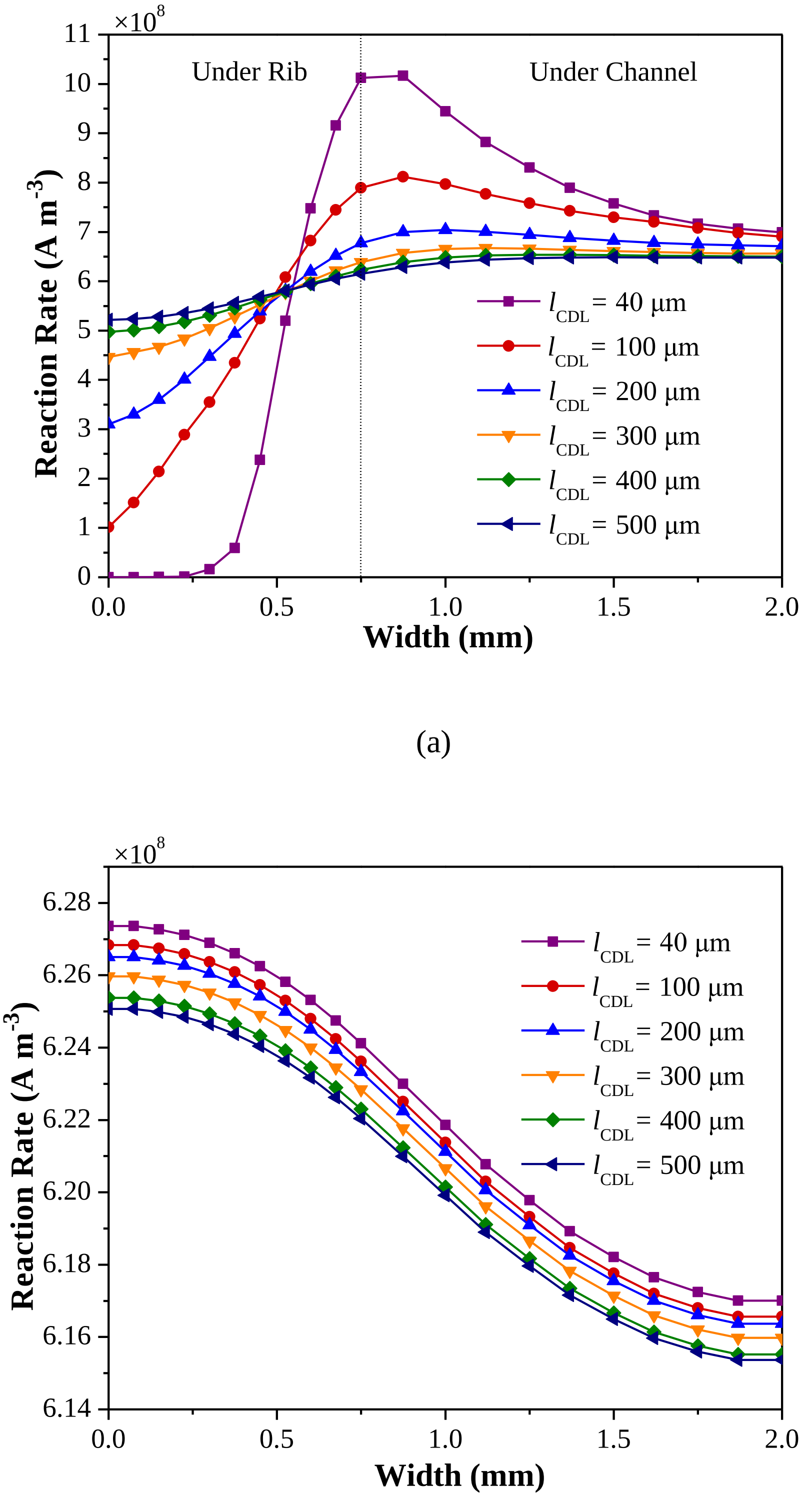

(a)

(b)

Fig.8 Reaction rate distribution on the middle of ELE/CCL interface at different CDL thickness.

(a) case A (b) case B

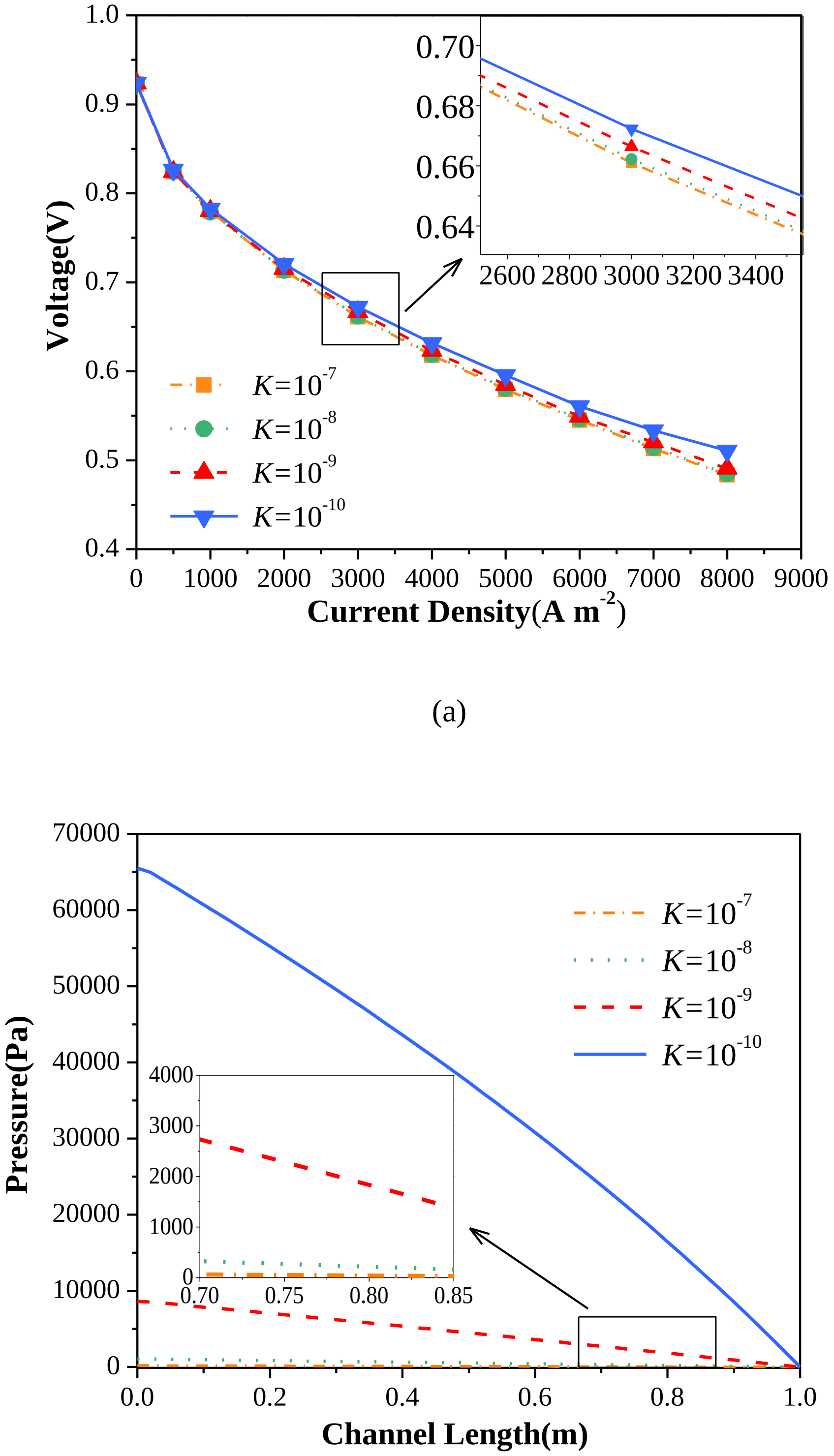

(a)

(b)

Fig.9 Effect of foam permeability at current density of 5000 A m^{-2}.
(a) on the cell performance; (b) on the pressure drop.

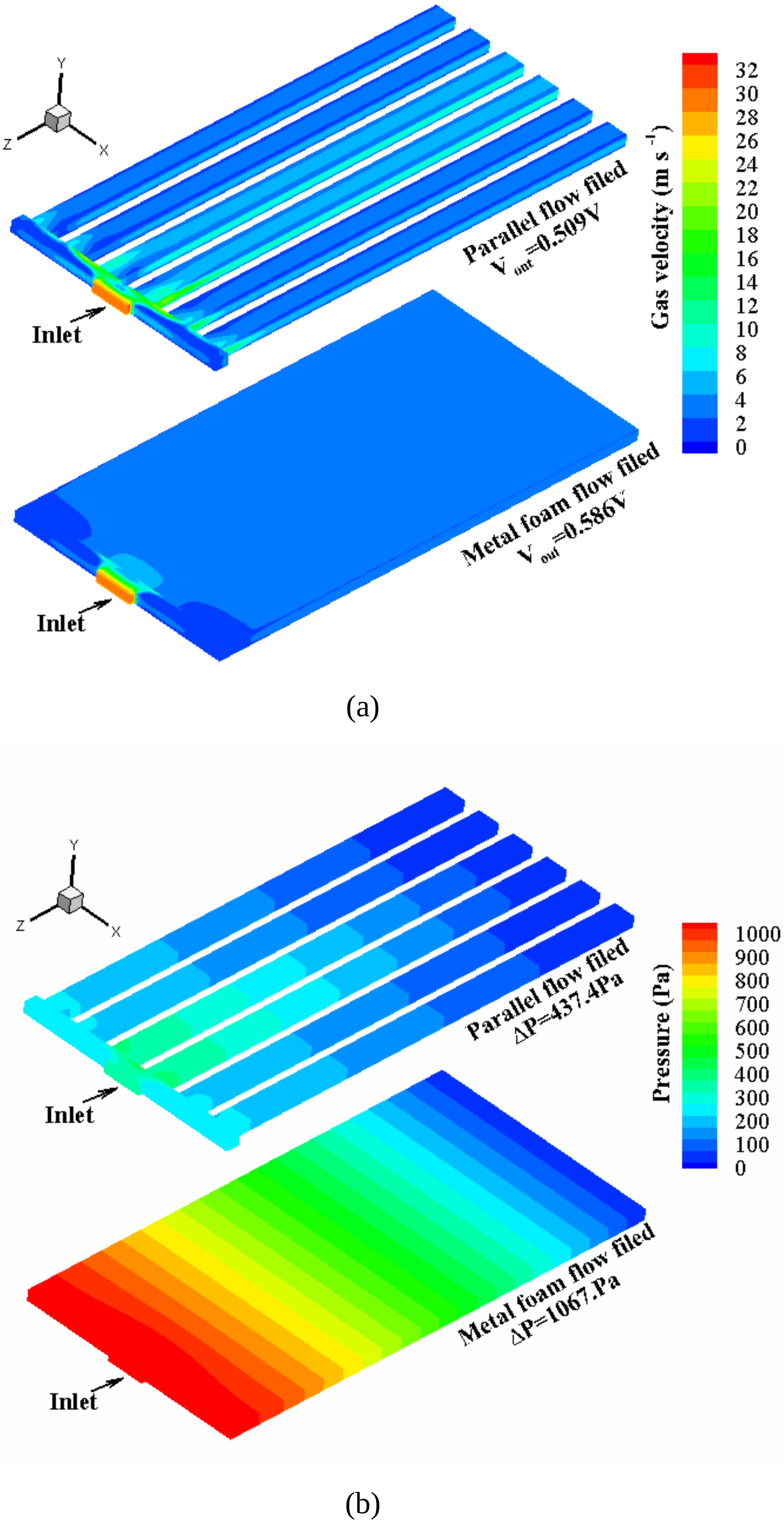

Fig.10 Velocity and pressure distributions of two different cathode flow fields.

(a) velocity distribution. (b) pressure distribution.

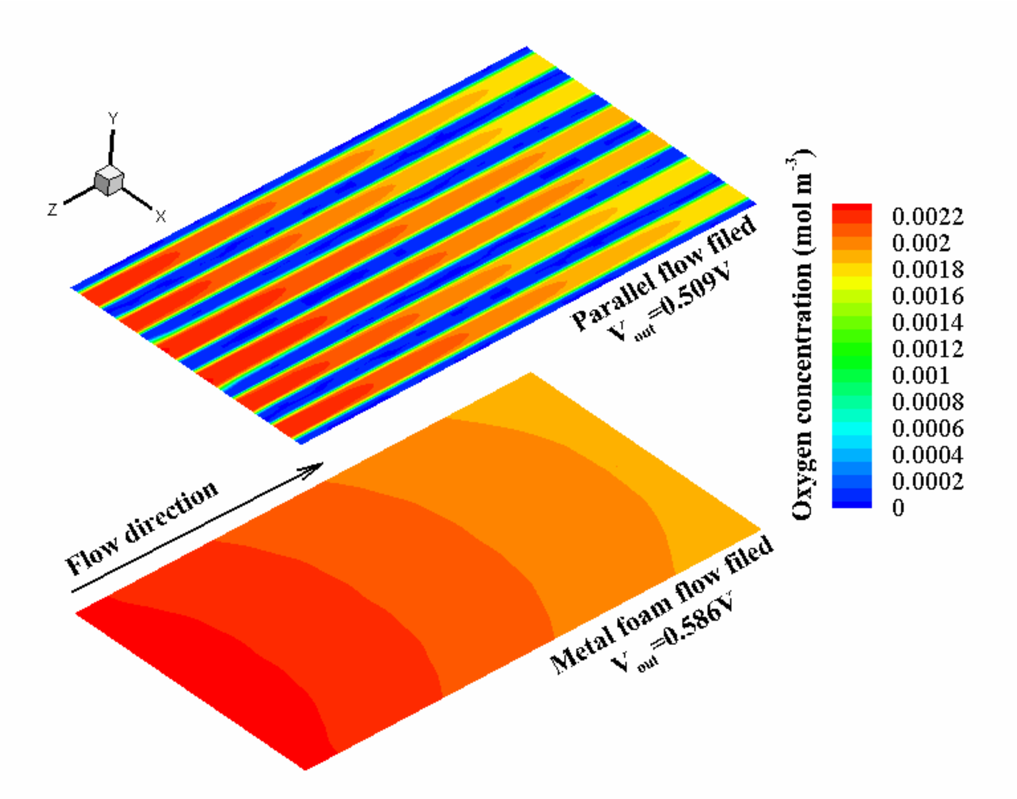

Fig.11 Oxygen concentration distribution on the ELE/CCL interface of two different flow fields.

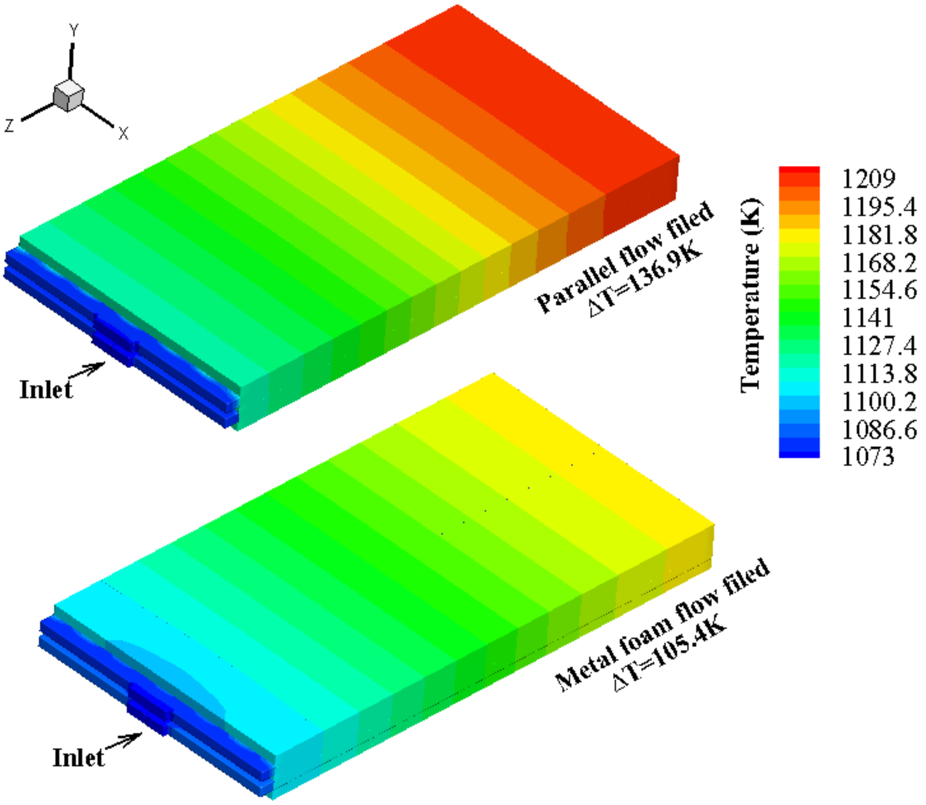

Fig.12 Temperature distribution of SOFC with two different flow field.